

Utilization of Nanosize Spent Oil Shale for Water Treatment: Application of Top-Down Nanonization Technology for Solid Residues

Adnan Abu-Surrah

The Hashemite University

Yahya Al-Degs (✉ yahyasalem1971@gmail.com)

The Hashemite University <https://orcid.org/0000-0002-9555-7594>

Research Article

Keywords: Top-Down Nanonization, Spent Oil Shale, Microsize, Nanosize, Textural Analysis, Sorption

Posted Date: April 5th, 2022

DOI: <https://doi.org/10.21203/rs.3.rs-1424011/v1>

License:  This work is licensed under a Creative Commons Attribution 4.0 International License.

[Read Full License](#)

Abstract

Since the dawn of nanoscience, producing nanomaterials in a simple, low-cost, and high-yield manner has been a major issue. For the commercial manufacturing of nanomaterials, various bottom-up and top-down methodologies have been established thus far. High energy dry ball milling has been widely used for the production of diverse nanomaterials, nanograins, nanoalloys, and nanocomposites. Physical grinding of inorganic solid wastes into nanosize (1-100 nm) seems to improve their industrial applications particularly as water adsorbent. Application of nanosize spent oil shale to sequester phenol is addressed in the current research. The collected spent oil shale (SiO_2 and Al_2O_3 making 45% of the material) has microstructure with average particle size of 56.6 μm . The dry grinding was performed in a vibrating ball mill at various grinding time (5-150 min) while keeping the grinding parameters constant including number of balls, ball size, mass, vibration frequency and amplitude. Upon grinding, the mean particle diameter of the bulk material was reduced to 191.8 and 85.2 nm using 0.5 and 0.1 mm grinding balls, respectively. To assess the influence of physical grinding, textural parameters are measured in addition to other chemical tests including specific surface area, pore volume, particle size distribution, X-ray fluorescence, pH_{PZC} , and phenol uptake. Although nanosize particles (85.2 nm) perform better than bulk material for phenol uptake, they underwent serious aggregation at $\text{pH} > 2$ and ionic strength > 1.0 mM. Hence, the 191.8 nm size is selected to assess the effect of mechanical grinding on sorption kinetics and equilibrium sorption capacity toward phenol as common pollutant.

Introduction

Nanomaterials have emerged as an exciting class of materials that are in high demand for a range of practical applications. Materials are defined as nanomaterials if their size or one of their dimensions is in the range of 1 to 100 nm (Baig et al., 2022; Marques et al. 2021; Trotta and Mele 2019; Sharifi et al. 2012; Kreyling et al. 2010). Currently, nanotechnology is rapidly evolving and becoming part of almost every field related to materials chemistry (Marques et al. 2021; Sharifi et al. 2012). The field of nanotechnology is evolving every day, and now powerful characterization and synthesis tools are available for producing nanomaterials with better-controlled dimensions (Trotta and Mele 2019). Nanotechnology is an excellent example of an emerging technology, offering engineered nanomaterials with the great potential for producing products with substantially improved performances. Currently, nanomaterials find many promising applications including biosensors, Li ion batteries, paints, surface coatings by physical/chemical vapor deposition, cosmetics, H_2 storage devices, CO_2 capture/conversion, dielectrics and water purification (Jian et al. 2019; Trotta and Mele 2019; Lu et al. 2016a; Lu et al. 2016b; Abu-Surrah et al. 2015; El-Ghanem et al. 2014)

Experimentally, there are two approaches that often used for preparation of nanomaterials which known as bottom-up and top-down (Trotta and Mele 2019). Bottom-up approaches, which often produced homogeneous nano-scale materials, use chemical or physical forces operating at the nanoscale to assemble basic units (atoms & molecules) into larger structures or particles (Trotta and Mele 2019; Cao et al. 2017; Wu et al. 2011). Chemical vapor deposition, solvothermal/hydrothermal, sol-gel, and soft/hard

templating are the main Bottom-up approaches (Cao et al. 2017; Wu et al. 2011). In top-down approaches, the bulk or the large size materials are reduced into nanostructured materials and this accomplished by mechanical milling, etching, electro-explosion and sputtering (Trotta and Mele 2019; Cao et al. 2017). Among the earlier methods, mechanical grinding is an effective process for producing materials at the nanoscale level (< 100 nm) from bulk materials (Moys 2015; Yadav et al. 2012; Cho et al., 2009). Moreover, mechanical milling is an effective to produce blends of different phases and production of nanocomposites (Yadav et al. 2012; Cho et al., 2009). In fact, mechanical grinding is often used to produce oxide- and carbide-strengthened aluminum alloys, wear-resistant spray coatings, aluminum/nickel/magnesium/copper-based nanoalloys, and many other nanocomposite materials (Yadav et al. 2012). In addition to ball milling, sputtering is an effective process to produce nanomaterials via bombarding solid surfaces with high energy particles such as plasma or gas. There is no single nano grinding mill; at the same time, not all milling techniques can produce nanoparticles. Ball wet/dry media and jet mills are often used to reduce large particles to nanosize range 1-100 nm (Cho et al. 2009). Nanoparticles would be fabricated using wet or dry milling methodologies and each method has its own advantages and disadvantages (Moys 2015). Nanoparticles can agglomerate, making them difficult to disperse upon grinding, however, wet milling can handle particles agglomeration by encapsulating each nanoparticle in the liquid slurry

(Trotta and Mele 2019; Zhuang et al. 2016; Moys 2015; Cho et al. 2009). Moreover, wet milling was more stable and efficient for producing nanosize materials from solid residues (Cho et al. 2009). Dry methods, such as jet milling, can achieve the desired particle size without using milling media but consume more energy (Cho et al. 2009; He and Forssberg 2007; Bilgili et al. 2006; Bilgili et al. 2004). Compared to top-down, bottom-up synthesis processes are often generate high-quality nanoparticles but they are expensive and need highly advanced and specialized equipment (Trotta and Mele 2019). There are many analytical methods can be applied to identify the size of nanomaterial in their solid state including scanning electron micrograph SEM, N₂-adsorption method, laser diffractometer, scanning tunneling microscopy, atomic force microscopy (Al-Ajji and Al-Ghouti 2021; Sadegh et al. 2017; Kyzas and Matis 2015). However, zeta potential, rate of aggregation, and hydrodynamic particle size in solution (under different conditions) can studied using dynamic light scattering spectroscopy (Jian et al. 2019).

Removal of organic and inorganic pollutants by engineered nanosize materials was studied using TiO₂, Al₂O₃, and different nanoshapes of nanotubes activated/graphene was evaluated (Sadegh et al. 2017; He and Forssberg 2007). In fact, removal of pollutants by nanosize adsorbents complicated due to possible aggregation of particles which may reduce the intrinsic sorption ability of the original nanomaterial (Trotta and Mele 2019). For instance, removal of organic compounds by nanosize Al₂O₃ was highly dependent on pH and ionic strength due their influence on particle aggregation (Lu et al. 2016b). However, sorption capacity of nanomaterial would be higher (compared to the bulk material) apparently due to large surface area and surface charge (Trotta and Mele 2019). It should be noted here that many research articles investigated the adsorption affinity of engineered nanomaterials (TiO₂, Al₂O₃, Fe₃O₄, MnO₂, MgO, ZnO, carbon nanotubes, and Graphite oxide) different pollutants (Sadegh et al. 2017; Kyzas and Matis

2015), however, very limited research on using nanomaterial, prepared by top-down, as water adsorbent is addressed (Al-Ajji and Al-Ghouti 2021).

In the current research, ball dry milling will be used to generate nanosize spent oil shale and further tested to remove phenol from solution under different conditions of pH and ionic strength. The "as-received" spent oil shale has an average particle diameter of 56.6 μm which is suitable for direct dry milling to end up with nanosize materials of potential industrial applications. Nanonization of spent oil shale is carried out using dry milling methodology which consumed lower energy compared to other methods and producing particles close to typical nanosize (1-100 nm). Surface characterization of nanonized particles in their solid state will be measured by BET method while particle size range by laser diffractometry. Effect of aggregation on nanosize particles (< 100 nm) is assessed using light dynamic scattering method. As a model pollutant, adsorption efficiency of nanosize spent oil shale toward phenol is tested and compared with bulk or micro-size material.

Methodology

Spent oil shale and grinding into nanosize material

JOSCO Company contributed approximately 3.0 kilogram of discarded oil shale. JOSCO is a major shale oil extraction firm with extensive experience (Al-Saqarat et al. 2017). Due to the large proportion of calcium carbonate in local oil shale, the material was reacted with 0.1 M HCl for 5.0 hours to remove carbonates and concentrate other components such as Si and Al oxides. The residue was washed multiple times with water and dried at 130 °C after acid treatment. Spent oil shale was crushed and mechanically sieved into the following ranges: >106, 63–106, 45–63, and < 45 μm and the mass percentages of the collected fractions were 11.4, 55.8, 21.7 and 11.1%, respectively. Each fraction was analysed for particle size distribution. Nanonization of the material was carried using 45–63 μm fraction following dry-milling methodology. A commercial beads mill instrument (Planetary Mill PULVERISETTE 7 premium line) was used to grind spent oil shale using 0.1 and 0.5 mm size zirconium balls. Initially, A 5.0 ml of dried spent oil shale ($D_{50} = 45 \mu\text{m}$) was placed inside the grinding bowl (20 ml) along with the grinding balls. The bowl was fastened onto the sun dial before the start of grinding operation. By crushing and grinding at extremely high speed, the sample was comminuted in small size particles. The maximum rotational speed of grinding using this technology would reach up to 1100 rpm which result in a high increase of the kinetic energy of grinding particles. The grinding duration to the nanoscale was ranged from 60–180 min. In this work, grinding of spent oil shale was carried out using 0.1 and 0.5 mm zirconium oxide balls while the process time was 60 min. Nanonization by 0.1 mm balls was carried out after grinding with 0.5 mm which is necessary to get ultrafine particles by increasing contact area upon grinding process. At the end of grinding, the content of the bowl was removed and stored in glass container in preparation for adsorption and physiochemical tests.

Surface Characterization

Scanning electron microscopy SEM (FEIINSPECT- F50-SEM, The Netherlands) was used to view the surfaces of the samples. Chemical composition was determined with X-ray fluorescence XRF (Shimadzu XRF-1800 Sequential X-Ray Fluorescence Spectrometer, Japan). The textural characteristics (specific surface area, pore volume and pore size distribution) of the spent oil shale nanosize forms were determined using standard N₂-adsorption techniques (Nova 4200e, Surface Area and Pore Size Analyser). The specific surface area was estimated with the multipoint BET method. The total pore volume was calculated from the N₂ gas adsorbed at P/P₀ 0.95 while micropore volume was estimated with the Dubinin-Radushkevich method. The average pore diameter (APD) was obtained with the Barrett-Joyner-Hanlenda BJH approach. A laser diffractometer was used to measure particle size distribution of solid particles (Microtrac Zetatrac, Microtrac, Particle Size Analyzer, USA). The pH_{zpc} (pH at zero point of charge) of adsorbents was estimated using potentiometric titration as outlined in the literature (Davranche et al. 2003). Two suspensions were prepared by adding 1.0 g of adsorbent in CO₂-free 300 mL of 0.1 M NaNO₃ as the supporting electrolyte. One suspension is directly titrated with 0.1 M HNO₃ while the other with 0.1 M NaOH. After 5 min of stirring, titrations were performed over the 3–11 to avoid any solid solubilisation and this was necessary due to alkaline nature of spent oil shale.

Aggregation studies of nanosize spent oil shale

Dynamic light scattering DLS was used to study the aggregation behaviour nanosize particles by measuring hydrodynamic particle diameter. A Nano ZS 90 (Malvern Instruments) was used to monitor particle size distributions at different pH and ionic strength (KCl) conditions. The experimental conditions in DLS tests were kept consistent with adsorption experiment before the DLS analysis. Each sample (with different solution chemistry) was measured in duplicate.

Adsorption tests of phenol by nanonized spent oil shale

Adsorption and kinetic tests: Initially, effect of pH and ionic strength on phenol uptake by nanonized materials was investigated by contacting 50 mg adsorbent with 50 mL solution containing 100 mg/L phenol. In general, the ratio 40–50 mg/50mL is recommended to get stable nano-suspension and avoid aggregation at higher dosages (Jian et al. 2019; Lu et al. 2016b). pH was adjusted by adding 0.1 M HCl or NaOH to before adding adsorbent to cover the range (2.0–12.0) while ionic strength was adjusted by adding NaCl to final range 0–15 mM. All mixtures were agitated at 25 C in a thermostated shaker for 240 min to attain equilibrium. The particles of oil shale were separated by centrifugation at 15000 g for min and the clean supernatant was measured at 270 nm. The equilibrium concentration of phenol was estimated from the following calibration equation: $A = 0.0167C + 0.0004$ ($R^2 = 0.9988$) which derived from Beer's law by plotting A_{270nm} (λ_{max} of phenol is 270 nm) against concentration (0.1–55.0 mg/L). Spectral measurements were carried out with a UV-Vis spectrophotometer (Cary 3E UV-Vis spectrophotometer, Varian, USA). Adsorption rate of phenol was carried out at 25 °C, pH 6.0, initial concentration 100 mg/L, and solid-to-liquid ratio of 30mg/50mL. The samples were removed at pre-selected time spacing, analysed as outlined above, and phenol uptake at time t was estimated as: $q_t = ((C_0 - C_t) \times V) / m$, where C_0 , C_t , V , and m are the initial concentration (mg/L), phenol concentration (mg/L) at time t , volume of

solution (L), and mass of spent oil shale (g), respectively. A concentration-variation adsorption methodology was used to study the effect of nanonization of spent oil shale on equilibrium uptake of phenol from solution. The test was conducted as follows: 300 mg dried adsorbent was contacted with 100 mL phenol solution of different concentration (0-100 mg/L) at (pH 6.0, 25 °C) for 240 min to attain equilibrium. The equilibrium time was determined from separate kinetic tests. The pH was periodically checked and adjusted if necessary. After equilibrium, phenol was measured as outlined above. The amount of phenol removed by adsorbent q_{ads} was estimated as: q_{ads} (mg/g) = $((C_o - C_e) V) / m$, C_e is the equilibrium phenol concentration (mg/L). All reagents were of analytical quality and doubly distilled water was used in the tests. Different kinetic and isotherm models were applied to present phenol uptake from solution by nano or microsize materials.

Mathematical Models

Adsorption kinetics: Kinetics of phenol uptake was presented by pseudo-first (Eq. 1) and second order (Eq. 2) models (Al-Zawahreh et al. 2021; Akar et al. 2014)

$$q_t = q_e(1 - e^{-k_1 t}) \quad (1)$$

$$q_t = \frac{tk_2 q_e^2}{1 + tk_2 q_e} \quad (2)$$

Where q_t and q_e are the amounts of dye removed at time t and equilibrium time, respectively. The parameters k_1 (min^{-1}) and k_2 ($\text{g mg}^{-1} \text{min}^{-1}$) are the first-order and the second order rate constants ($\text{g mg}^{-1} \text{min}^{-1}$).

Adsorption isotherms: Among known models, Langmuir, Freundlich and Sips were used to present phenol isotherms. Langmuir isotherm is (Al-Zawahreh et al. 2021; Issa et al. 2014; Al-Degs et al. 2008; Al-Degs et al. 2003)

$$q_e = \frac{Q_L K_L C_e}{1 + K_L C_e} \quad (3)$$

where Q_L (mg/g) and K_L (L/mg) are the maximum sorption capacity 9mg/g) and the affinity constant. Freundlich isotherm expression defines the heterogeneity of the surface as well as the exponential distribution of the active sites on the surface (Al-Zawahreh et al. 2021; Issa et al. 2014):

$$q_e = K_F C_e^{1/n_F} \quad (4)$$

where K_F is the Freundlich constant and can indicate uptake capacity while $1/n$ measures favourability of the process and both are system specific constants. Sips model is a three-parameter model that often

applied to present sorption isotherm data over a wide concentration range. Sips model has the validity in localizing the adsorption without the adsorbate-adsorbate interaction (Al-Zawahreh et al. 2021):

$$q_e = \frac{Q_s K_s C_e^{n_s}}{1 + K_s C_e^{n_s}} \quad (5)$$

where Q_s (mg/g), K_s (L/mg) ^{n_s} , and n_s are Sips maximum adsorption capacity (mg/g), Sips equilibrium constant, and the model exponent. The relative error of prediction ($REP\%$) was used as a criterion to select the optimum model as equilibrium data was fitted by more than one model. $REP\%$ is estimated as (Al-Zawahreh et al. 2021):

$$REP\% = 100 \times \left(\frac{\sum_{i=1}^n (q_{i,pred} - q_{i,act})^2}{\sum_{i=1}^n (q_{i,act})^2} \right)^{1/2} \quad (6)$$

where $q_{i,pred}$, $q_{i,act}$ and n are predicted sorption value, actual sorption value, and the number of experimental points, respectively. Lower $REP\%$ indicates better model fitting to the data.

Results And Discussion

Physicochemical characterization of spent oil shale: Solid state characterization

Before discussing the activity of nanosize particles in solution, physicochemical characterization results were discussed for different sizes of spent oil shale. The tests including SEM, XRF, FTIR, textural properties (SSA and porosity), particle size distribution, size effect of grinding balls, and effect grinding time on nanostructure of the resulted materials. Figure 1 depicts the electron micrographs of bulk SOS and other nanosize form, which make it possible to qualitatively estimate the size range and shape of these particles

As viewed in Fig. 1A, the particles of SOS have non homogenous and irregular shapes which resulted upon heating the oil shale up to 500 °C while extracting kerogen. Generally, the picture indicates the presence of particles with a diameter of less than 40 µm and particles much more than 40 µm. The SEM picture recorded for the finest particles (85.2 nm as measured by laser technology) indicates the clear effect of nano-grinding, as it produced relatively homogeneous particles (compared to raw material) with a diameter around 100 nm and less.

XRF and FTIR: In fact, the raw material has large amount of CaCO₃ along with Si and Al oxides. Hence, removal of carbonate mineral by acid dissolution was necessary to concentrate Si and Al improve

mechanical properties. For raw sample, XRF indicated that CaO, SiO₂, Al₂O₃, and Fe₂O₃ were the main oxides with mass content of 41.14, 16.41, 2.56, and 1.24%, respectively. Upon acid treatment, SiO₂, Al₂O₃, and Fe₂O₃ were notably increased to 33.4, 12.5 and 5.62%, respectively. The high increase in the earlier oxides was attributed to the elimination of carbonates from the solid matrix. The dissolution of carbonate mineral by acid treatment (Mashaal et al. 2021) and detection of polar surface functional groups (like Si-OH and Al-OH) which contributed to the surface charge of the adsorbent and removal of phenol can be detected by FTIR as shown in Fig. 2.

In fact, IR analysis was limited to SOS-191.8 nm as this adsorbent showed high sorption for phenol, hence detection of adsorbed solute is possible. The following IR bands were noticed in the spectrum of SOS-191.8 nm before after phenol uptake: 1011–1105, 879–881, 798–802, 709–710, 478–480 cm⁻¹. None of the earlier bands evidenced the presence of organic phenol on the surface but related to the structure of the material which mainly composed of Si, Al, and Fe as conformed by XRF. The strong and broad IR band located at 1011 and 1105 cm⁻¹ (Fig. 2A&B) with shoulders at 1161 and 1164 cm⁻¹ are assigned to the TO and LO modes of the Si-O-Si asymmetric stretching vibrations (Darmakkolla et al. 2016). The strong band of Si-O-Si reflected the high concentration of SiO₂ in the sample which in agreement with XRF analysis. The IR bands at 881 (Fig. 2A) and 879 (Fig. 2B) cm⁻¹ are assigned to silanol groups. The IR bands at 798 and 802 cm⁻¹ were assigned to Si-O-Si symmetric stretching vibrations, while the bands (478 & 480 cm⁻¹) are attributed to O-Si-O bending vibrations. The bands appeared at 710 (Fig. 1A) and 709 cm⁻¹ (Fig. 2B) are attributed Al-O vibrations. The new IR bands that appeared upon phenol uptake (Fig. 1B) are 2530 and 2869 cm⁻¹ were attributed to C-H stretching in the organic solute. The bands appeared at 3620 and 3697 cm⁻¹ (Fig. 2A) are attributed to the intense -OH stretching (in Si-OH or Al-OH) (Darmakkolla et al. 2016). The involvement of the earlier -OH groups in phenol uptake is evidenced by reduction in their intensity in the IR spectrum of used adsorbent (Fig. 2B). The broad IR band at 3346 cm⁻¹ may evidence the presence of adsorbed water molecules. Moreover, significant stretching band at 3346 cm⁻¹ also indicated the O-H phenolic hydroxyl. The band 3346 cm⁻¹ would support the complexation of phenol with SOS and suggests that this contribution of H-bonding during the complexation of SOS-phenol may be worth development of water adsorbent.

Influence of grinding ball size on nanonization of spent oil shale

The development of ultrafine processing forms has lately been advanced in response to the need to manage low-grade finely dispersed solid wastes (Moys 2015). Blended media or centrifugal mills, which use progressively fine media and tactics of increasing control input that are not governed by gravity, are displacing ball grinders or mills. For ultra-fine processing (i.e., down to item sizes of less than 1–10 m), these tactics proved to be basic, increasing grinding rate while also demonstrating increased power productivity (Bilgili et al. 2004). Vertical blended mills such as the MetProTech and Deswik plants are potential competitors in the industry, and flat or horizontal grinders such as the IsaMill have been built with 3 MW control requirements. He and Forssberg investigated the impact of slurry rheology on blended

processing kinetics with molecule intermediate sizes as small as 4 m as part of their research (He and Forssberg 2007). At the same time, Bilgili and colleagues have achieved a nanoscale size of 30 nm, which is well within the normal nanoscale range (Bilgili et al. 2006). In the current work, nanonization of spent oil shale was accomplished using dry-milling using Planetary Mill PULVERISETTE 7. The experimental parameters for grinding process were mass ratio spent oil shale/zirconium beads, the rotor speed, and the bead size. The earlier factors can be adjusted by the instrument to achieve the optimum results, i.e, fine particle of size less than 100 nm. One of the main dry grinding parameters is the ratio ($V_{\text{grinding zone}} / V_{\text{voids}}$) and the efficiency of grinding is incensed by increasing the earlier ration (Moys 2015). A graphical presentation of mechanical milling by zirconia balls is depicted in Fig. 3.

In fact, the grinding rate in a mill is limited by the volume of the grinding zones in the mill (area b in Fig. 1). The beads are assumed to be a distance f apart, due to the presence of fine particles in the gap. Hence, the grinding zone (b) is then the circular bi-concave segment as shown in Fig. 3. The volume between the beads (d as shown in Fig. 1) is also important as it affects the final grinding efficiency. Particles outside this zone cannot be compressed by zirconia balls and hence will not be ground. It has been shown that, the ratio $V_{\text{grinding zone}} / V_{\text{voids}}$ (b and d in Fig. 1) can be correlated with the diameter of particles to be grinded and beads diameter as (Moys 2015):

$$\frac{V_{\text{Grinding-Zone}}}{V_{\text{voids}}} = 13.4 \left(\frac{d_{\text{particle}}}{d_{\text{beads}}} \right)^2 \quad (1)$$

In fact, Eq. 1 indicated that fine particles can be generated at low size of grinding balls and this factor should be carefully selected. Hence, the size of grinding balls used for nanonization has high influence on the size if the final product. Balls of smaller size can produce finer particles due to the high contact with solid particles. D_{10} , D_{50} , and D_{90} values obtained from particle size distribution profiles are provided in Table 1 and Fig. 4.

Table 1
Estimated D values of spent oil shale after nanonization at different sizes of grinding balls^a

Spent oil shale		Grinding - 0.5 mm balls ^c		Grinding - 0.1 mm balls ^d	
D value	Particle diameter (µm)	D value	Particle diameter (nm)	D value	Particle diameter (nm)
D_{10}^b	43.6	D_{10}	147.3	D_{10}	68.3
D_{50}	58.1	D_{50}	189.4	D_{50}	77.5
D_{90}	68.1	D_{90}	238.7	D_{90}	109.9
Arithmetic mean diameter	56.6 µm		191.8 nm		85.2 nm

- a. Grinding time 60 min
- b. $D_{10} = 43.6$ indicated that 10% of particles have diameter $\leq 43.6 \mu\text{m}$
- c. The size of zirconium balls is 0.5 mm diameter.
- d. The size of zirconium balls is 0.1 mm diameter.

As indicated in Table 1, spent oil shale have average particle diameter of $56.6 \mu\text{m}$ where 90% of particles has diameter less than $68.1 \mu\text{m}$. It should be recall that laser analysis was performed for the $45\text{--}63 \mu\text{m}$ fraction which present 22% of the examined sample. The formation of fine particles of spent oil shale was attributed the exposure a high temperature ($550 \text{ }^\circ\text{C}$) and pressure during retorting process (Al-Saqarat et al. 2017). Thus, instead of obtaining a normal bell-shaped distribution curve for the particle size distribution of SOS (Fig. 4A), double bell-shaped curves are obtained. As indicated in Fig. 4A, the first maxima occurs at a relatively smaller range ($70\text{--}140 \mu\text{m}$) of particle diameters while the second one positioned between 160 and $240 \mu\text{m}$. The presence of two peaks would indicate the unequal thermal distribution during grinding. In general, industrial composition of organic matters often generated restudies of diameter $0.2\text{--}90 \mu\text{m}$. Upon mechanical crushing, the mean particle diameter of was significantly reduced and nanosize material was produced. Moreover, sample grinding by smaller beads (0.1 mm) has been significantly reduce particle diameter to 85.2 nm , which is typically fall with nanosize range $1\text{--}100 \text{ nm}$ (Moys 2015). The interesting point was the normal bell-shaped distribution curve of the particles (Fig. 4B) that resulted upon nanonization. The normal distribution curve was expected due to the uniform grinding of the particles of spent oil shale. The best nanonization result was obtained using 0.1 mm balls with D_{10} , D_{50} , and D_{90} values of 68.3 , 77.5 , and 109.0 nm , respectively. The production of nanosize particles using 0.1 mm balls is attributed to high increase in the grading zone volume as indicated in Eq. 1. As can be estimated from Eq. 1, reducing the size of balls from 0.5 to 0.1 mm has been increased the grading zone 25 times which can be resulted in production of 85.2 nm particles. It seems that nanonization of the original material has been reflected on the apparent density of the material as depicted in Fig. 5.

As indicated in Fig. 3, the same mass of the material (Fig. 3A) has occupied double size after nanonization (Fig. 3B) which can reflect the high increase in surface charge upon nanonization.

Textural measurements of nanosize adsorbents and effect of grinding time

The main factors that can affect the particle size distribution of the material is grinding time (Arsoy et al. 2017). Hence, effect of grinding time on and particle size distribution and specific surface area was investigated for the particles obtained using 0.1 mm zirconia balls (Table 1). Particle size distribution including D_{10} , D_{50} and D_{90} and specific surface area as a function with grinding time is shown in Fig. 6.

Before starting the discussion, it is important to note that effect of grinding time on the particle size distribution and surface area of the resulting particles was performed on the initial particle size of 191.8 nm (Table 1). The reason for this selection is that the particles produced using 0.1 mm balls were in the

nanosize range (85.2 nm), which is important in this research. The results (Fig. 6A) showed that D10, D50, and D90 fractions were notably reduced with grinding time and over the period 20–60 min. After 60 min grinding, particle size distribution was not highly changed. Among fractions, D90 was highly reduced with size reductions of 50%, 37% and 33% for D90, D50 and D10 within the first milling hour, respectively. The large reduction in D90, i.e., the portion that containing the largest particles as shown in Table 1, can be attributed to the easier grinding of coarser particles compared to finer ones. Moreover, grinding coarser particles would insure higher grinding zone volume compared to voids area as anticipated in Eq. 1. Similar results were also obtained in literature (Arsoy et al. 2017; Liao, M. Senna 1992). The influence of grinding time on average particle diameter and specific surface area is depicted in Fig. 6B. In fact, specific surface area is a physical parameter which depends on particle size, density, and porosity of the solid material. Since the available surface area increases with decreasing particle size, an increase in surface area was observed upon grinding. As can be seen in Fig. 6B, the decrease in average particle size has been resulted in increase in the surface area of material. Highest surface area (38 m²/g) was reported at the lowest particle size (80 nm). It has been reported that specific surface area of aluminosilicate minerals would increase from 9.0 up to 24.0 m²/g (i.e., 2-fold increase) with changing particle size (Arsoy et al. 2017; Zbik and Smart 2005). Even there was no a large decrease increase particle size at longer grinding time, the surface area of grinded material kept increasing and this attributed to the nanosize structure of the grinded material. Moreover, this also be explained by conversion of closed pores into open pores and a consequent increase in the total pore volume during the grinding process (Arsoy et al. 2017; Zbik and Smart 2005). The influence of nanonization on specific surface area and porosity was studied using N₂-adsorption methodology. N₂-adsorption/desorption isotherms and BJH plots for SOS and 85.2 nm size are provided in Fig. 7. Moreover, physical parameters of are provided in Table 2.

Table 2
Textural parameters estimated N₂ isotherms for spent oil shale and other nanonized versions

Parameter	Adsorbent		
	Spent oil shale	Grinding – 0.5 mm balls	Grinding – 0.1 mm balls
S _{BET} ^a	16.7	23.5	36.4
S _{ext} ^b	-	6.41	14.2
S _{mic} ^c	16.7	21.8	25.3
V _t ^d	0.010	0.016	0.026
V _{mic} ^e	0.010	0.015	0.018
V _{mes} ^f	-	-	0.008
Average pore diameter ^g (nm)	2.41	2.73	2.85
Arithmetic mean particle diameter	56.6 μm	191.8 nm	85.2 nm
^a Specific surface area (m ² /g), multipoint BET method (El-Barghouthi et al. 2007).			
^b External surface area (m ² /g), t-plot method) (El-Barghouthi et al. 2007).			
^c Micropore surface area, t-plot method (Al-Degs et al. 2008; El-Barghouthi et al. 2007)			
^d Total pore volume (cm ³ /g) estimated at P/P ₀ = 0.95 (El-Barghouthi et al. 2007).			
^e Micropore volume (diameter < 2 nm) (cm ³ /g) estimated from Dubinin-Radushkevich method (Al-Degs et al. 2008).			

^f Mesopore volume (diameter: 2–50 nm) (cm³/g) estimated at P/P₀ range 0.40–0.95 (Al-Degs et al. 2008).

^g Barrett-Joyner-Hanlenda (BJH) method (El-Barghouthi et al. 2007).

Surface area is a physical property which depends on particle size and porosity of material. Since the available surface would increase with decreasing particle size, an increase in surface area was observed upon grinding. The increase in surface area upon grinding is attributed to the conversion of closed pores into open pores and a consequent increase in the total pore volume during the grinding process. As indicated in Fig. 7A&C, typical type-II isotherms were reported for micro and nanosize materials. Filling of micropores in both materials was achieved at low pressure P/P₀ ≈ 0.2. It seems that grinding particles to

nanosize has relatively increased the mesoporous structure of the material as indicated from the higher adsorbed amount of N_2 within the region (P/P_0 0.4–0.6) with values 9.0 and 23.0 cm^3/g for SOS and 85.2 nm size particles. In fact, the flatter region in the middle of the isotherm indicates the formation of a monolayer. At very low pressure, the micropores fill with nitrogen gas. At the knee, monolayer formation is beginning and multilayer formation occurs at medium pressure. At the higher pressures, capillary condensation occurs. In general, type II isotherm is often observed on non-porous solids or solids with diameter exceeding micropores and the later was the case in this work (Al-Zawahreh et al. 2021). As shown in Table 2, specific surface area of the raw material has been improved upon nanonization, more than 2-fold increase was reported upon grinding with 0.1 mm balls. Moreover, nanonization has increased external surface area, total pore volume, and little increase in mesoporosity of 0.1 mm-nanonized material. It seems that crushing the material has improved the physical surface area of the material with slight effect on the microstructure of the solid material. The estimated specific surface area of the adsorbents (density 1.12 g/cm^3) and assuming spherical particle were < 1, 28.3, and 63.0 m^2/g for raw, 191.8 nm size, and 85.2 nm size, respectively. Although the earlier areas were different from N_2 -values, they would reflect the large increase in external surface area with slight improvement in the internal structure. As indicated in Table 2 and Fig. 7B&D, the materials have microporous structure with average pore diameter of 2.41, 2.73 and 2.85 nm for SOS, 191.8 nm size, and 85.2 nm size, respectively. The slight increase in pore diameter of 85.2 nm size adsorbent would be attributed to the pores opening upon crushing. It is necessary to mention that adsorption performance of nanosize material in solution would be affected by many factors.

Sorption and aggregation behavior of SOS particles under different conditions

In fact, sorption behavior of phenol by different sizes of SOS was tested at different pHs and ionic strengths. Moreover, the results indicated that particle size has high influence on phenol retention especially for nanosize range (< 100 nm), hence, aggregation of particles was checked by measuring hydrodynamic particle size using dynamic light scattering.

Effect of pH on phenol uptake and particles aggregation

Removal of phenol was tested at wide pH range 2.0–12.0, 120 mg/L concentration, ionic strength 0–15 mM, and S/L ratio of 40 mg/50 mL and this is necessary to minimize aggregation of nanosize particles at adsorbent dosage (Jian et al. 2019; Lu et al. 2016b). Moreover, surface charge was measured for different particle sizes. The results are shown in Fig. 8.

For nanosize materials, S/L ratio should be maintained as low as possible to prevent particles aggregation (Baalousha et al. 2016) and most studies conducted sorption test over the range (10–250 mg)/50mL (Jian et al. 2019; Lu et al. 2016b; Wang et al. 2015; Wang and Shih 2011). In this work, phenol uptake was tested at S/L 10–60 mg/50mL and at 60 mg/L pollutant. In general, phenol uptake was increased and stabilized at S/L ratio of 50mg/50mL. Hence all sorption tests were performed at S/L ratio 50mg/50mL.

Although particle grinding ended up with nano size particles (Table 1), high phenol uptake was achieved at 191.8 nm but not 85.2 nm particles and this was attributed to aggregation of the later particles. However, the interesting point in Fig. 8A is that both 85.2 and 191.8 nm outperformed bulk SOS and this was attributed to the higher surface area and pore volume of the former adsorbents (Table 2). Among adsorbents, 191.8 nm-size particles achieved the best removal (35 mg/g) at pH 6.0. In fact, nanosize particles aggregates much higher than other sizes which negatively reflected on phenol uptake from solution (Baalousha 2017). In fact, the aggregation behavior of nanomaterials is highly affect with pH, ionic strength, chemistry of adsorbate and complexing agents (Jian et al. 2019). Hence, aggregation behavior of SOS-85.2 nm was examined at the same sorption conditions as shown in Fig. 8B. As indicated in Fig. 8, the particles involved high aggregation with pH and is also reported in the literature (Jian et al. 2019; Raza et al. 2016). At pH 2.0, the nanosize material has been aggregated to generate aggregates of hydrodynamic diameters H-d of 1000 nm (33%) and 3000 nm (3%). In fact, the nanosize particles encountered high aggregation in solution as H-d was increased from 85.2 to around 1000 nm at pH 2. At pH 4.5, more aggregation was observed and the average H-d was increased to 2000 nm with intensity of 60%. The high aggregation at 4.5 would be attributed to the high reduction of surface charge as this pH is very close to pH_{ZPC} . At basic medium (pH 10), the particles underwent intense aggregation with H-d of 2500 and 5000 of intensities 55 and 12%, respectively, this large increment on H-d would be attributed to the reduction in dielectric layer at high ionic solution as predicted from DELVO theory (Baalousha 2017). In general, the nanosize particles of SOS (85.2 nm) demonstrated high aggregation with pH and similar behavior was reported for certain nanomaterials (Jian et al. 2019). Accordingly, the gradual reduction in phenol uptake (Fig. 8A) for 85.2 nm with pH was attributed to aggregation of particles which supposed to reduce surface area and pore volume and adsorbent-adsorbate repulsion as will be explained later. The fate of nanomaterial in adsorption medium is dependent on particle shape, pH, ionic strength, chemistry of adsorbate (Raza et al. 2016). In fact, the aggregation behavior of nanomaterials has been tested at different pH, ionic strength, and complexing agents (Jian et al. 2019; Lu et al. 2016b; Raza et al. 2016). For instance, TiO_2 nanomaterial has high stability (i.e., go not highly aggregate) at acidic pH and over a wide salt level but aggregate at neutral pH and low concentration of salt (Lu et al. 2016b). In the same line, aggregation kinetics of different nanomaterials were tested using dynamic light scattering of UV spectroscopy and published data indicating that increasing ionic strength increase the rate of aggregation of nanomaterial (Baalousha et al. 2013). Aggregation kinetics of nanomaterials is often controlled by: a) electrostatic forces among particles (diameter 1-100 nm), and b) electrostatic interferences which depends on ionic strength, solution pH, stabilizing agent of nanoparticle, and coating thickness (Raza et al. 2016; Baalousha et al. 2013). The results provided in Fig. 8A indicated that both pH and particle size have significant influence on phenol uptake. For the examined pH range, the bulk material and SOS-191.8 nm manifested the same adsorption trend and the best uptake was reported over the range (4–8) and a high reduction observed at $pH > 10.0$. Moreover, phenol removal at pH 2.0 was not high. Both electrostatic interaction and H-bonding were involved in solute uptake from solution. As indicated from IR spectra both Si-OH and Si-O-Si were the main surface functional groups and the ionization of the particles with pH are shown in Fig. 8C. As shown in Fig. 8C, the point of zero charge pH_{ZPC} was 4.3 and above this point the surface ionizes to carry negative charge ($Si-O^-$) and

positive charge (Si-OH_2^+) at $\text{pH} < 4.3$. pH_{zpc} was close to pure SiO_2 (4.0) and this was expected as silica making a large fraction of the material. As SOS and SOS-191.8 nm did not encounter serious aggregation at tested pHs then the mechanism of phenol retention is explained as following: a) At $\text{pH} 4-8$, the H-bonding between neutral phenol ($\text{p}K_a = 10$) and polar Si-OH (especially in the range 3.5–4.5) is the dominating mechanism while above 4.5 another mechanism like van der Waals forces will dominate the process, b) At $\text{pH} < 4.0$, surface protonation is started and this will reduce phenol uptake via H-bonding keeping van der Waals forces the controlling mechanism, and c) $\text{pH} > 10.0$, surface ionization is strengthened leading to electrostatic repulsion between phenolate ions and the surface (Fig. 8). The best retention for SOS and SOS-191.8 nm was at $\text{pH} 6$ and hence van der Waals forces was more dominate than H-bonding. Despite the similarity in the adsorption behavior, SOS-191.8 nm removed 3.7-folds phenol from solution (Fig. 8, $\text{pH} 6.0$) than SOS and this thank to its finer particle size and high surface area (Table 2). In fact mechanical grinding leading to finer particles and maximize surface charge as shown in Fig. 8, the maximum surface charge was reported for 191.8 nm at $\text{pH} 7.3$ with a value of $150 \mu\text{mol}(-)/\text{m}^2$) which was 4 times higher than the bulk material. In summary, SOS-191.8 nm was the winner adsorbent to remove phenol as it has higher surface area compared to bulk and did not encounter serious aggregation like nanosize form (85.2 nm).

Effect of ionic strength on phenol uptake and particles aggregation

Removal of phenol was tested at different ionic strength 0–15 mM at S/L ratio 50 mg/50 mL and this is necessary to minimize aggregation of nanosize particles as mentioned earlier. The results are shown in Fig. 9.

As indicated in Fig. 9A, particle size has inconsistent effect on phenol uptake. For bulk SOS and 191.8 nm size, removal of phenol was increase upon adding KCl and no substantial effect was observed at concentration higher than 10 mM. The interesting point was observed for nanosize particles (85.2 nm) which exhibited a substantial reduction with KCl where phenol uptake went down to 15 mg/g at 15.0 mM NaCl. Another important factor that affect aggregation of nanosize particles was ionic strength as shown in Fig. 9B. Undoubtedly, the nanosize particles (56.6 nm) underwent intense aggregation in solution which increased H-d to 6000 nm at 15.0 mM and this negatively affected phenol uptake from solution (Fig. 9B). The results of dynamic light scattering (not provided) that reported for bulk and 191.8 nm did not show serious aggregation with ionic strength and this can explain their comparable behavior toward phenol uptake (Fig. 9A). In fact, effect of ionic strength on phenol removal was tested without adjusting solution pH. The equilibrium pH of solutions was within the range 3.9–4.3 and at this range both phenol ($\text{p}K_a 10.0$) and solid particles ($\text{pH}_{\text{zpc}} 4.2$) are neural form, hence the contribution of electrostatic attraction is not dominant. The earlier observation can is in agreement with literature in that aggregation of nanomaterial is highly increase with the concentration of added salt (Baalousha et al. 2013). For the bulk material (56.6 μm) and 191.8 nm particle size, the increase in phenol uptake would be attributed to the salt-effect as the salt will reduce phenol solubility and hence improve its uptake (Wang et al. 2016). The

high affinity of 191.8 nm compared to the bulk one is attributed to the higher surface area/porosity (Table 1) which attract more phenol from solution.

Adsorption kinetic and isotherm

As indicated in Fig. 8B&9B, nanosize particles, although perform better than bulk material, they underwent serious aggregation at $\text{pH} > 2$ and ionic strength > 1.0 mM. Hence, the 191.8 nm size was picked up to assess the effect of mechanical grinding on sorption kinetics and equilibrium sorption capacity against bulk material. Sorption kinetics and equilibrium isotherms were measured to get a better picture on phenol uptake by bulk and 191.8 nm size. The results are depicted in Fig. 10 while parameters of the tested models are summarized in Tables 3&4.

As indicated in Fig. 10A, phenol uptake was higher for SOS 191.8 nm as indicated from its steeper slope over the initial time of interaction (10 min). Moreover, the higher surface area of SOS 191.8 nm (Table 2) offer more contact with solution which ended up with faster equilibrium time, 60 against 180 min for the bulk material.

Table 3

Pseudo-first and pseudo-second order model parameters for phenol uptake by different sizes of oil shale. $q_e(\text{exp})$: experimental sorption value at equilibrium (mg g^{-1}); $q_e(\text{model})$: equilibrium sorption value predicted from the model (mg g^{-1}); k_1 : pseudo first order model constant (min^{-1}); k_2 : pseudo second order model constant ($\text{g mg}^{-1} \text{min}^{-1}$); h sorption rate ($\text{mg g}^{-1} \text{min}^{-1}$) = $k_2 q_e^2$; REP%: relative error of prediction.

Sorbent	$q_e(\text{exp})$	Pseudo-first order model ^a			Pseudo-second order model ^b			
		k_1	$q_e(\text{model})$	REP%	k_2	$q_e(\text{model})$	h	REP% ^c
SOS 56.6 μm	12.32	0.0247	12.19	2.4	0.0018	14.69	0.39	1.7
SOS 191.8 nm	37.43	0.0827	35.86	6.3	0.0029	39.07	4.43	1.8

As indicated in Table 3, kinetic curves of phenol were fairly presented by Pseudo-second order model which showed more flexibility compared to Pseudo-first order model as indicated from the lower REP% values. The magnitudes of sorption rate h , which estimated from second order model, were 0.39 and 4.43 $\text{mg g}^{-1} \text{min}^{-1}$ for SOS and SOS 191.8 nm, respectively, and this jump is equivalent to an 11-fold increase in the rate of phenol sorption. Rate constants k_1 , estimated by Pseudo-first order model, also indicated faster uptake of phenol by SOS 191.8 nm (Table 3).

As shown in Fig. 10B, typical L-type isotherm was obtained. In solution, L-type isotherms are most typically encountered in solute sorption. The initial shape of the equilibrium curve follows the basic premise that the higher the solute concentration, the greater the adsorption capacity, until the number of possible adsorption sites is occupied. Comparable isotherm shapes were reported for phenol uptake by

carbon nanomaterials (de la Luz-Asunción et al. 2015). The parameters of examined models are summarized in Table 4.

Table 4

Isotherm parameters for phenol adsorption. Q_L : Langmuir maximum capacity (mg g^{-1}); K_L : Langmuir constant (L g^{-1}); K_F : Freundlich constant (L g^{-1}); n : Freundlich coefficient; Q_s : Sips saturation value (mg g^{-1}); K_s : Sips model constant; n_s : Sips model exponent.

Adsorbent	Langmuir			Freundlich			Sips			
	Q_L	K_L	REP%	K_F	n	REP%	Q_s	K_s	n_s	REP%
SOS 56.6 μm	10.62	1.82	6.1	6.19	4.37	10.3	10.71	1.76	0.97	5.4
SOS 191.8 nm	38.36	2.22	11.2	21.33	4.92	12.0	39.29	1.89	0.88	7.4

Among tested models, Sips was the more suitable to present phenol uptake by both adsorbents with REP% 5.4–7.4. In fact Sips model is a combination of both Langmuir and Freundlich isotherms, which is often applied to predict the heterogeneity of the adsorption systems as well as to circumvent the limitations associated with the increased concentrations of the adsorbate of Freundlich model. This, in turn, leads to the production of an expression that have a finite limit at high concentration (Al-Zawahreh et al. 2021). However, both Langmuir and Sips models were fairly predicated the maximum retention of phenol from solution. The maximum saturation values, as predicted from Sips model, were 10.71 and 39.29 mg/g for SOS and SOS 191.8 nm, respectively. The performance of SOS 191.8 nm for phenol uptake (39 mg/g) was rather comparable to nanomaterial that derived from carbon with maximum retention of 31 mg/g (de la Luz-Asunción et al. 2015). In addition, the exponents of Ferundlich model (4.37 and 4.92) indicated the favorability of sorption process over the concentration range and heterogeneity of adsorbents (Al-Zawahreh et al. 2021; Al-Degs et al. 2008).

Conclusions

Mechanical grinding of solid residues of spent oil shale converted the bulk material (56.6 μm) into two fine particles one in the nanosize range (85.2 nm) and another one close to nanorange (191.8 nm). The mechanical grinding has notably increased surface area and pore volume and this opened the way to examine the adsorption capacity of these substances in the water. Although nanosize particles (85.2 nm) performed better than bulk material to remove phenol, they exhibited significant aggregation at $\text{pH} > 2$ and ionic strength > 1.0 mM. Because it has a larger surface area than bulk and does not experience substantial aggregation like nanosize form, adsorbent with a particle size of 191.8 nm won the competition to remove phenol (85.2 nm). In fact, nanomaterial (1-100 nm) undergo serious aggregation in solution and this may limit their application as adsorbent. However, particle sizes more than 100 nm can be perform better in solution due to modest aggregation.

Declarations

Ethics approval and consent to participate

Not applicable

Consent for publication

Not applicable

Availability of data and materials

The datasets used and/or analysed during the current study are available from the corresponding author (Y.S. Al-Degs) upon request.

Conflicts of Interest

The authors declare no conflict of interest

Author Contributions

A.S. Abu-Surra: Conceptualization, Methodology, Writing – review & editing.

Y.S. Al-Degs: Methodology, Writing – review & editing.

Funding

The authors declare that no funds, grants, or other support were received during the preparation of this manuscript

Acknowledgments

Dr Al-Degs thank Mr. Bassem Nasrallah (Chemistry Department, Hashemite University, Jordan) for the continuous technical support represented by the spectroscopic analyzes as well as the compositional analysis of spent oil shale.

References

1. Abu-Surrah A, Jawad S, Al-Ramahi E, Hallak A, Khattari Z (2015) Effect of multi-walled carbon nanotubes aspect ratio and temperature on the dielectric behavior of alternating alkene-carbon monoxide polyketone nanocomposites. *Physica B: Condensed Matter* 463:76–81
2. Akar S, Sayin F, Turkyilmaz S, Akar T (2014) Multivariate optimization of the decolorization process by surface modified biomaterial: Box-Behnken design and mechanism analysis. *Environ Sci Pollut Res* 21:13055–13068
3. Al-Ajji M, Al-Ghouthi M (2021) Novel insights into the nano-adsorption mechanisms of crystal violet using nano-hazelnut shell from aqueous solution. *J Wat Process Eng* 44:102354

4. Al-Degs Y, El-Barghouthi M, El-Sheikh A, Walker G (2008) Effect of solution pH, ionic strength, and temperature on adsorption behavior of reactive dyes on activated carbon. *Dyes Pigmen* 77:16–23
5. Al-Degs Y, Tutunji M, Baker H (2003) Isothermal and kinetic adsorption behaviour of Pb²⁺ ions on natural silicate minerals. *Clay Miner* 38:501–510
6. Al-Saqarat B, Ibrahim K, Musleh F, Al-Degs Y (2017) Characterization and utilization of solid residues generated upon oil and heat production from carbonate-rich oil shale. *Env Earth Sci* 76:264
7. Al-Zawahreh K, Barral M, Al-Degs Y, Paradelo R (2021) Comparison of the sorption capacity of basic, acid, direct and reactive dyes by compost in batch conditions. *J Env Manag* 294:113005
8. Arsoy Z, Ersoy B, Evcin A, Icduygu M (2017) Influence of dry grinding on physicochemical and surface properties of talc. *Physicochem Probl Miner Process* 53:288–306
9. Baalousha M (2017) Effect of nanomaterial and media physicochemical properties on nanomaterial aggregation kinetics. *NanoImpact* 6:55–68
10. Baalousha M, Nur Y, Römer I, Tejamaya M, Lead J (2013) Effect of monovalent and divalent cations, anions and fulvic acid on aggregation of citrate-coated silver nanoparticles. *Sci Total Environ* 454–455:119–131
11. Baalousha M, Sikder M, Prasad A, Lead J, Merrifield R, Chandler T (2016) The concentration-dependent behaviour of nanoparticles. *Environ Chem* 13:1–3
12. Baig N, Kammakakam I, Falath W (2022) Nanomaterials: a review of synthesis methods, properties, recent progress, and challenges. *Mater Adv* 21:1821
13. Bilgili E, Hameym R, Scarlett B (2004) Production of pigment nanoparticles using a wet stirred mill with polymeric media. *China Particuol* 2:93–100
14. Bilgili E, Hamey R, Scarlett B (2006) Nano-milling of pigment agglomerates using a wet stirred media mill: elucidation of the kinetics and breakage mechanisms. *Chem Eng Sci* 61:149–157
15. Cao J, Qin C, Wang Y, Zhang H, Zhang B, Gong Y, Wang X, Sunc G, Bala H, Zhang Z (2017) Synthesis of g-C₃N₄ nanosheet modified SnO₂ composites with improved performance for ethanol gas sensing. *RSC Adv* 7: 25504–25511
16. Cho K, Chang H, Kil D, Kim B, Jang H (2009) Synthesis of dispersed CaCO₃ nanoparticles by the ultrafine grinding. *J Ind Eng Chem* 15:243–246
17. Darmakkolla S, Tran H, Gupta A, Rananavare S (2016) A method to derivatize surface silanol groups to Si-alkyl groups in carbon-doped silicon oxides. *RSC Adv* 6:93219
18. Davranche M, Lacour S, Bordas F, Bollinger J (2003) An easy determination of the surface chemical properties of simple and natural solids. *J Chem Edu* 80:76–78
19. de la Luz-Asunción M, Sánchez-Mendieta V, Martínez-Hernández A, Castaño V, Velasco-Santos C (2015). Adsorption of phenol from aqueous solutions by carbon nanomaterials of one and two dimensions: kinetic and equilibrium studies. *J. Nanomater* 405036
20. El-Barghouthi M, El-Sheikh A, Al-Degs Y, Walker G (2007) Adsorption behaviour of anionic reactive dyes on H-type activated carbon: Competitive adsorption and desorption studies. *Sep Sci Technol* 42:

21. El-Ghanem H, Abdul Jawad S, Al-Saleh M, Hussain Y, Abu-Surrah A (2014) Electrical impedance spectroscopic study of CNT/ethylene-alt-CO/propylene-alt-CO polyketones nanocomposite. *J Macromol Sci B* 53: 878–892
22. He M, Forssberg E (2007) Rheological behaviours in wet ultrafine grinding of limestone. *Miner Metall Process* 24:19–29
23. Issa A, Al-Degs Y, Al-Ghouti M, Olimat A (2014) Studying competitive sorption behavior of methylene blue and malachite green using multivariate calibration. *Chem Eng J* 240: 554–564
24. Jian J, Zhang C, Wang F, Lu X, Wang F, Zeng E (2019) Effect of solution chemistry and aggregation on adsorption of perfluorooctanesulphonate (PFOS) to nano-sized alumina. *Environ Pollut* 251: 425–433
25. Kreyling W, Semmler-Behnke M, Chaudhry Q (2010) A complementary definition of nanomaterial. *Nano Today* 5:165–168
26. Kyzas G, Matis K (2015) Nanoadsorbents for pollutants removal: A review. *J Molecu Liq* 203: 159–168
27. Liao J, Senna M (1992) Thermal behavior of mechanically amorphized talc. *Thermochim Acta* 197:295–306
28. Lu X, Deng S, Wang B, Huang J, Wang Y, Yu G (2016b) Adsorption behavior and mechanism of perfluorooctane sulfonate on nanosized inorganic oxides. *J Colloid Interf Sci* 474:199–205
29. Lu J, Liu D, Yang X, Liu H, Liu S, Tang H, Zhao Y, Cui F (2016a) Sedimentation of TiO₂ nanoparticles in aqueous solutions: influence of pH, ionic strength, and adsorption of humic acid. *Desa Wat Treat* 57: 18817–18824
30. Marques A, Vale M, Vicente D, Schreck M, Tervoort E, Niederberger M (2021) Porous silica microspheres with immobilized titania nanoparticles for in-flow solar-driven purification of wastewater. *Global Challenges* 2000116.
31. Mashaal K, Al-Degs Y, Al-Zawahrah S, Saleh A (2021) Extraction and fractionation of organic matters from Jordanian-origin oil shale under different operational parameters. *Petro Sci. Technol.* 1–21
32. Megiel E (2017) The role of nanomaterials as effective adsorbents and their applications in wastewater treatment. *J Nanostruct Chem* 7:1–14
33. Moys M (2015) Grinding to nano-sizes: Effect of media size and slurry viscosity. *Miner Eng* 74:64–67
34. Raza G, Amjad M, Kaur I, Wen D (2016) Stability and Aggregation Kinetics of Titania Nanomaterials under Environmentally Realistic Conditions. *Environ Sci Technol* 50:8462 – 8472
35. Sharifi S, Behzadi S, Laurent S, Forrest M, Stroeve P, Mahmoudi M (2012) Toxicity of nanomaterials. *Chem. Soc. Rev.* 41:2323–2343.
36. Trotta F, Mele A (2019) *Nanosponges: Synthesis and Applications*. Wiley – VCH
37. Wang S, Qiao N, Yu J, Huang X, Hu M, Ma H (2016) Effect of ionic strength on the adsorption behavior of phenol over modified activated clay. *Desa Wat Treat* 57:4174–4182

38. Wang F, Shih K (2011) Adsorption of perfluorooctanesulfonate (PFOS) and perfluorooctanoate (PFOA) on alumina: Influence of solution pH and cations. *Wat Res* 45:2925–2930
39. Wang F, Shih K, Leckie J (2015) Effect of humic acid on the sorption of perfluorooctane sulfonate (PFOS) and perfluorobutane sulfonate (PFBS) on boehmite. *Chemosphere* 118:213–218
40. Wu X, Lu G, Wang L (2011) Shell-in-shell TiO₂ hollow spheres synthesized by one-pot hydrothermal method for dye-sensitized solar cell application, *Energ Environ Sci* 4:3565
41. Yadav T, Yadav R, Singh D (2012) Mechanical Milling: a Top Down Approach for the Synthesis of Nanomaterials and Nanocomposites, *Nanosci Nanotechnol* 2: 22–48
42. Zbik M, Smart R (2005) Influence of dry grinding on talc and kaolinite morphology: inhibition of nano-bubble formation and improved dispersion. *Miner Eng* 18:969–976
43. Zhuang S, Lee E, Lei L, Nunna B, Kuang L, Zhang W (2016) Synthesis of nitrogen-doped graphene catalyst by high-energy wet ball milling for electrochemical systems. *Int. J. Energy Res.* 40:2136–2149

Figures

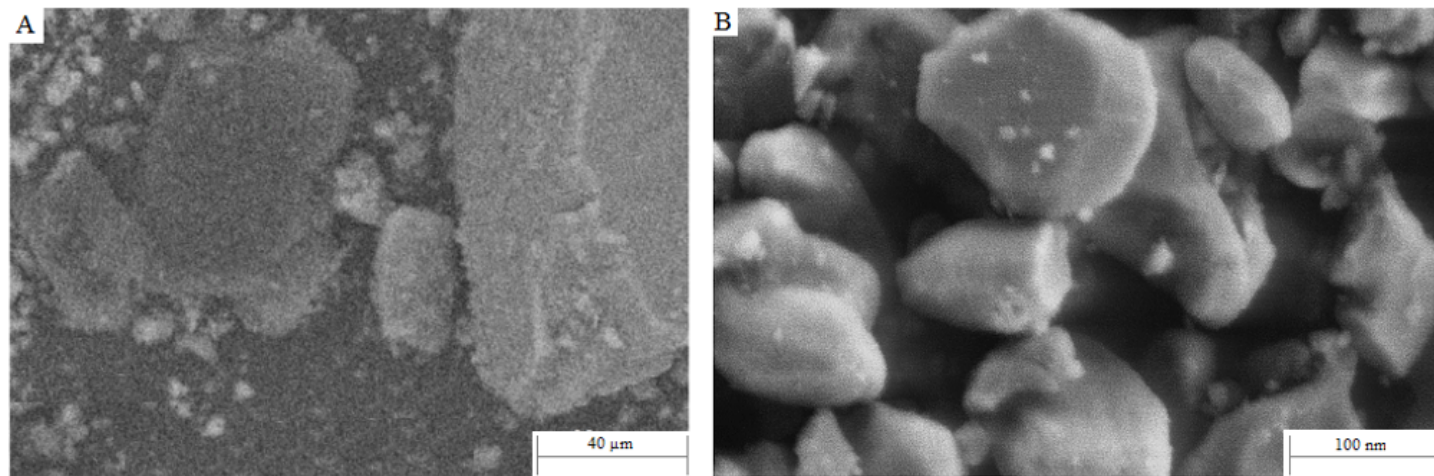


Figure 1

SEM of SOS (A) and SOS-85.2 nm (B) samples

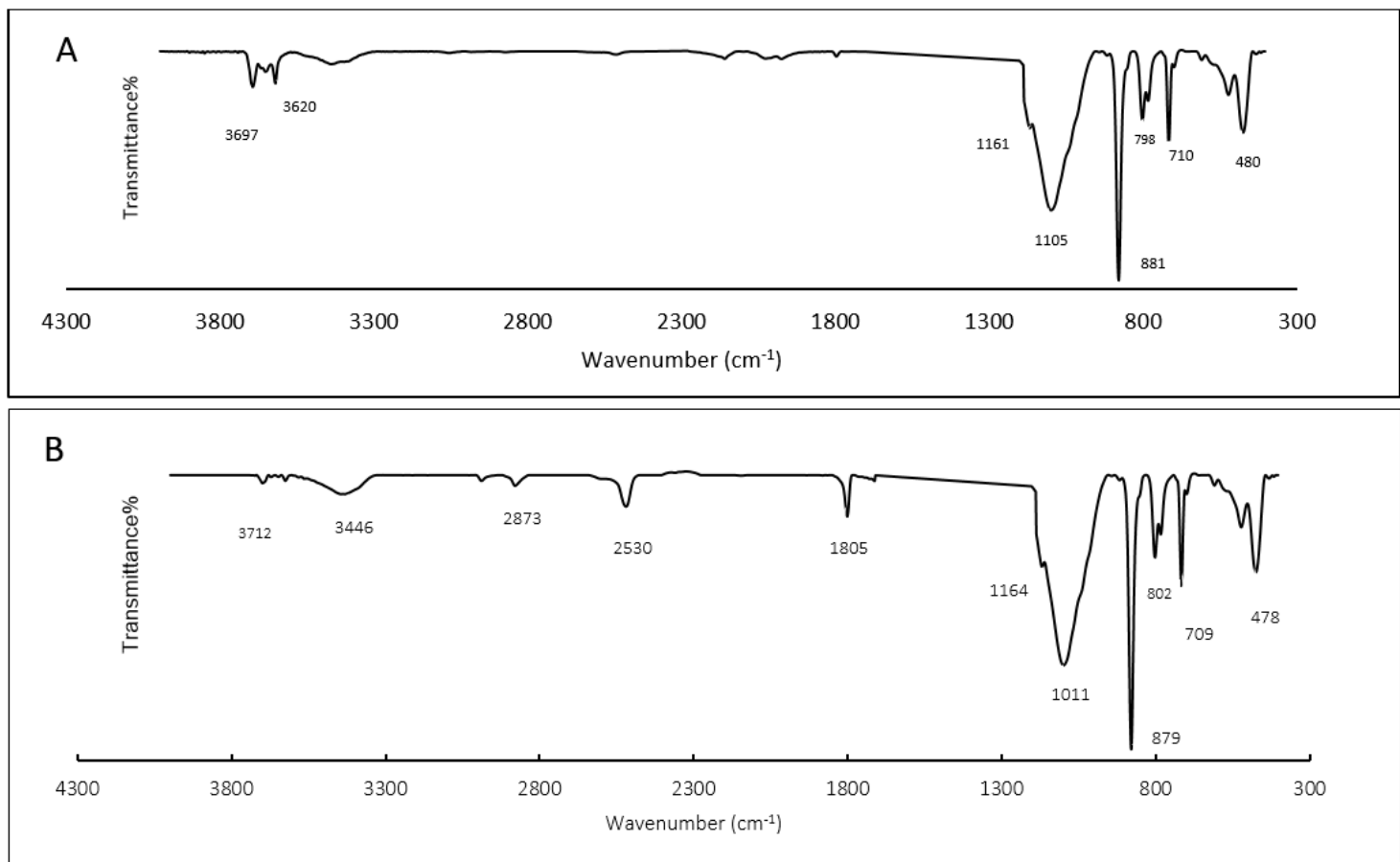


Figure 2

FTIR of SOS-191.8 nm before (A) and after phenol retention (B)

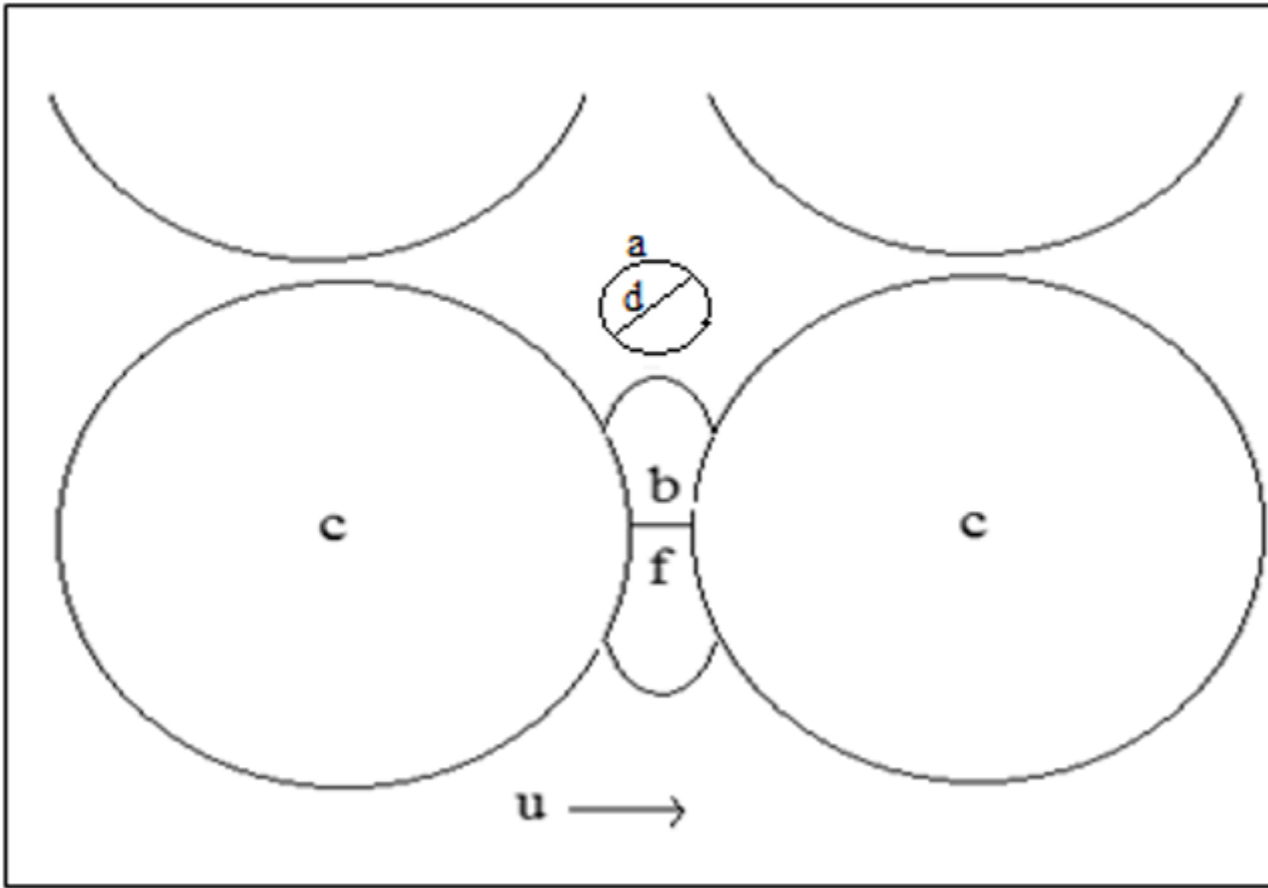


Figure 3

Grinding zone (**b**) for particle (**a**) of size d , between two balls (**c**) which are a distance **f** apart and are approaching each other at a velocity **u**.

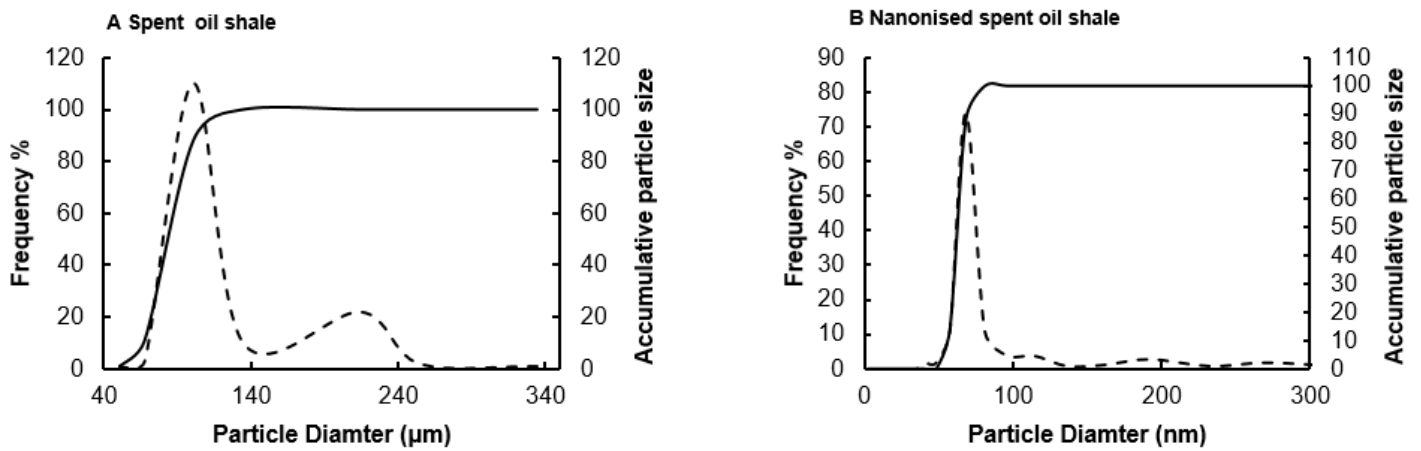


Figure 4

Laser particle size distribution of spent oil shale and nanosize products using 0.1 mm grinding balls.



Figure 5

Effect of nanonization on the physical appearance of spent oil shale **A** 0.432 g Bulk material (56.6 μm) and **B** 0.432 g nanonized material using 0.1 mm zirconia balls (85.2 nm).

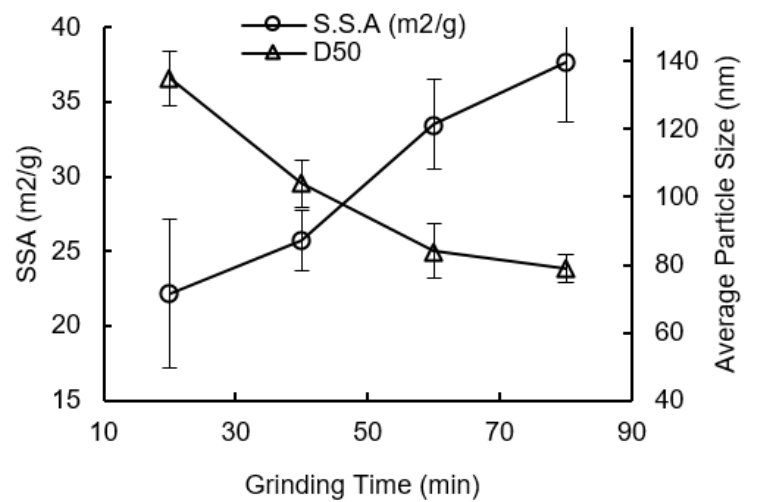
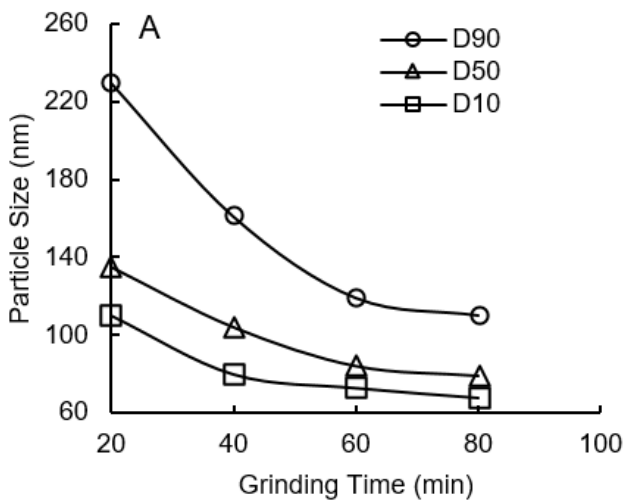


Figure 6

Effect of grinding time on particle size distribution (A) and specific surface area of nanosize particles (B).

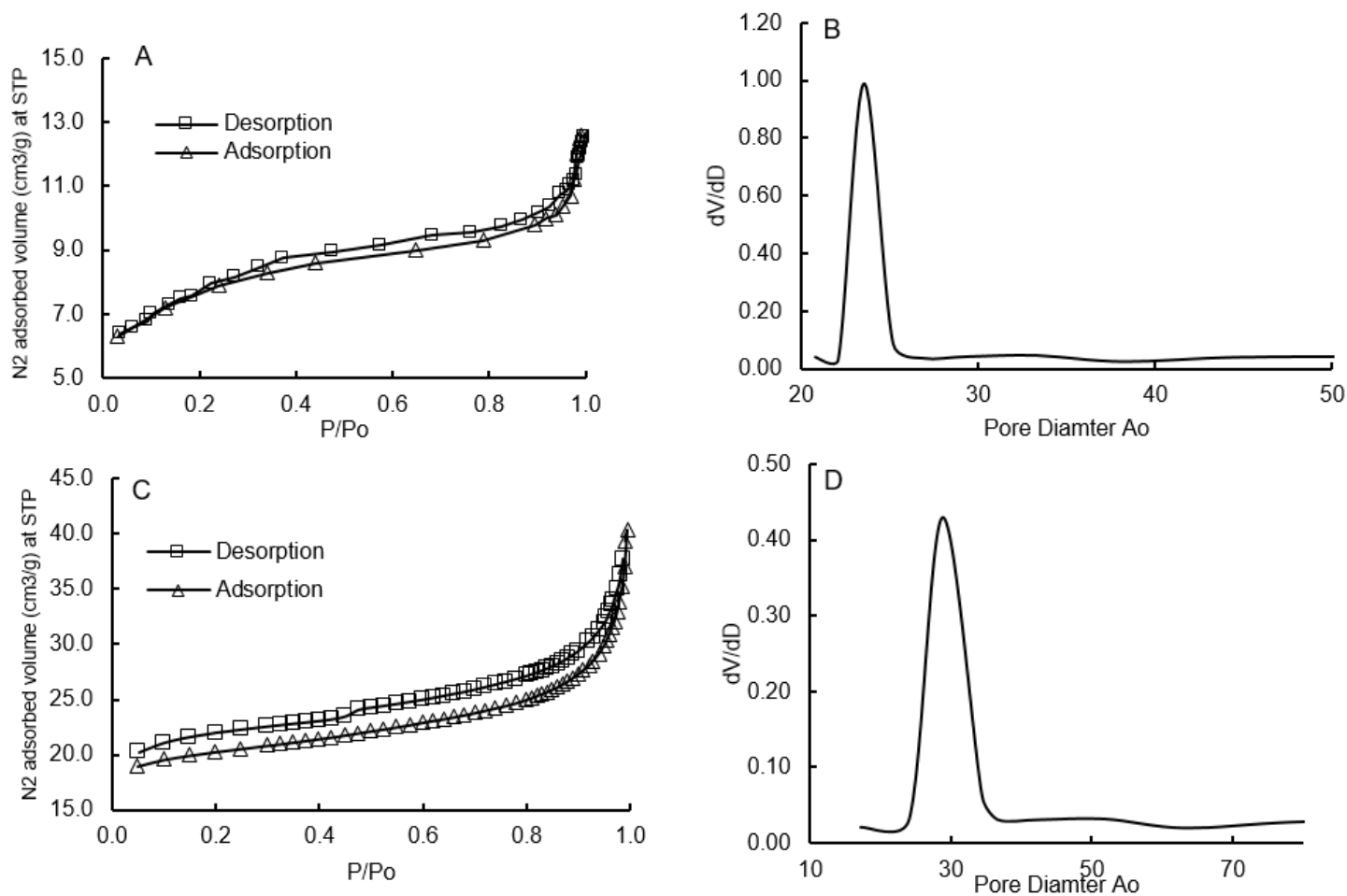


Figure 7

N₂ adsorption-desorption isotherms and BJH plots of SOS (A & B) and nanonized SOS using 0.1 mm balls (C & D)

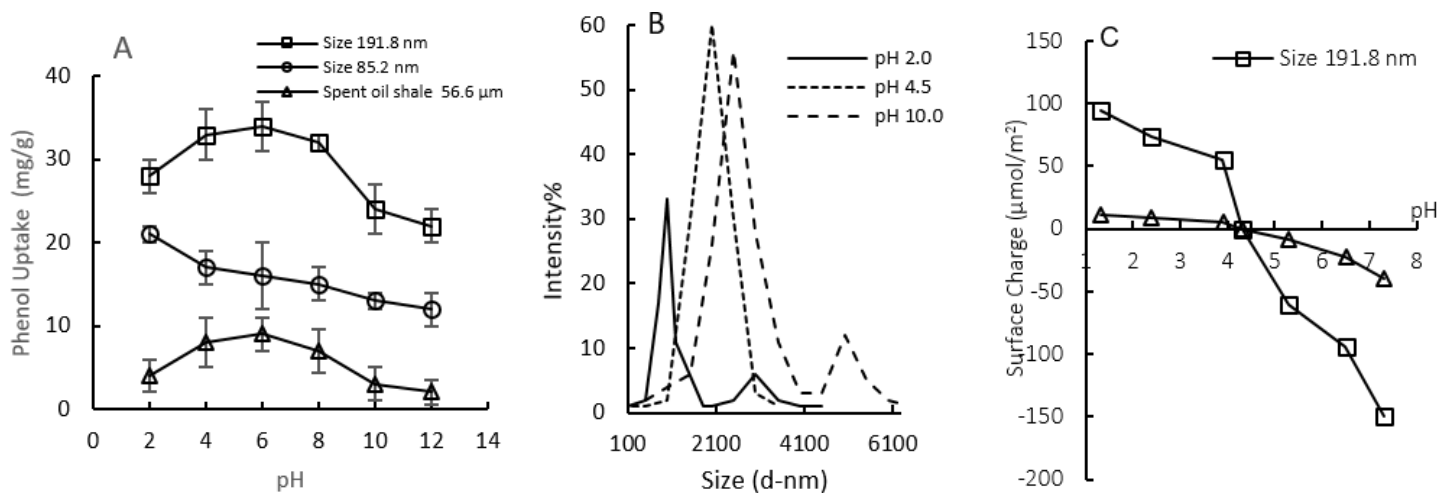


Figure 8

Effect of pH on phenol uptake **A** Intensity-based particle size distribution of SOS-85.2 nm at different pH using dynamic light scattering **B** Developed surface charge with pH **C**.

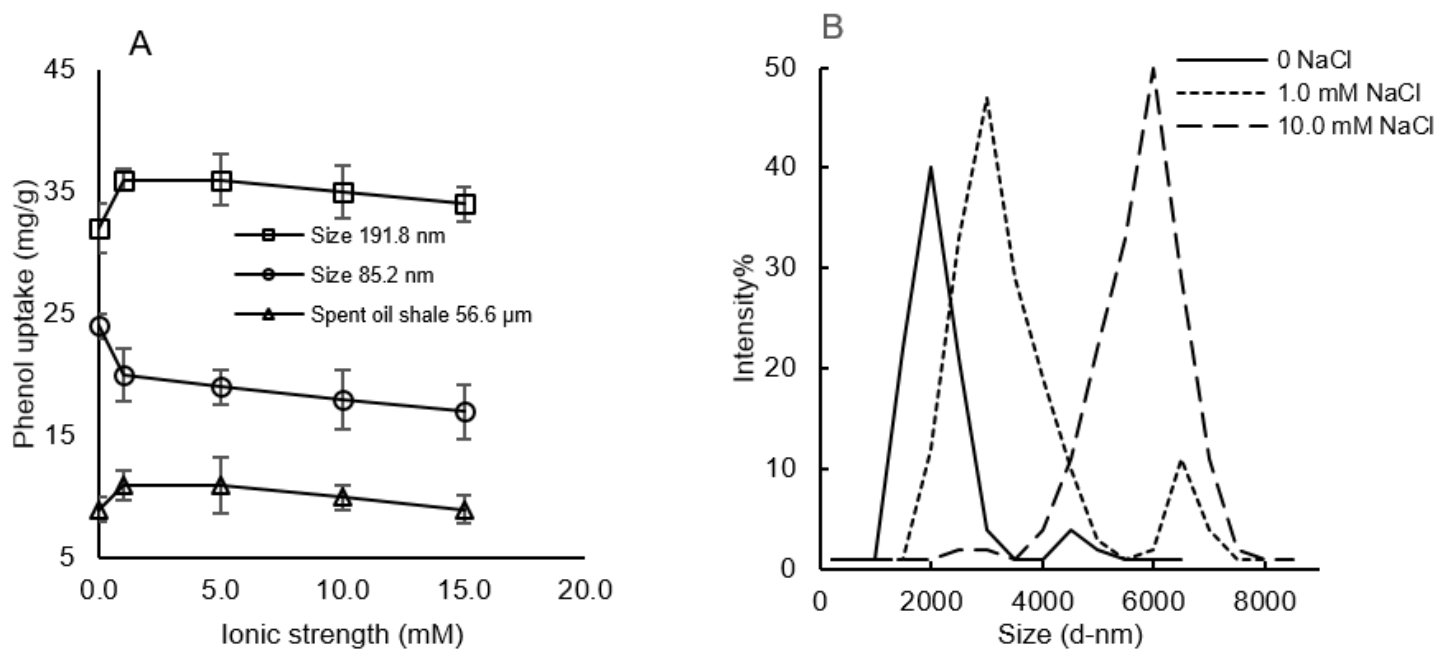


Figure 9

Effect of ionic strength on phenol uptake **A** Intensity-based particle size distribution of SOS-85.2 nm at different NaCl concentration using dynamic light scattering **B**

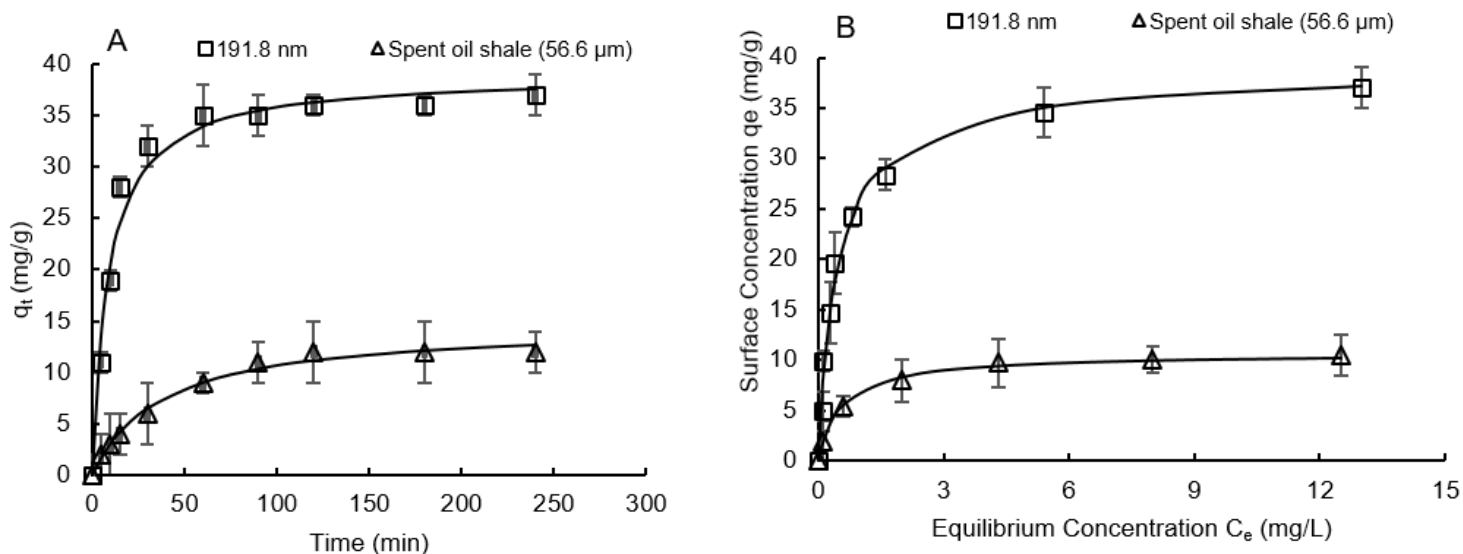


Figure 10

Kinetics of phenol uptake by spent oil shale of different particle size **A** and equilibrium isotherms **B**. Kinetics: concentration 60 mg/L phenol and agitation speed 120 rpm. Isotherms: concentration ranges 5-75 mg/L (for 191.8 nm size) and 1-25 mg/L (for bulk material), and agitation time 250 min. All tests performed at S/L ratio 50mg/50mL, pH 6.0, and 25 °C ($\pm 2^\circ$ C). In Fig 10A and 10B the dashed lines presented Pseudo-second order and Sips models, respectively.